A MULTI-WAVELENGTH STUDY OF THE JET, LOBES, AND CORE OF THE QUASAR PKS 2101–490

The Astrophysical Journal, 755:174 (15pp), 2012 August 20 doi:10.1088/0004-637X/755/2/174

A MULTI-WAVELENGTH STUDY OF THE JET, LOBES, AND CORE OF THE QUASAR PKS 2101−490

L. E. H. Godfrey[1,2], G. V. Bicknell[2], J. E. J. Lovell[3,4,5], D. L. Jauncey[3], J. Gelbord[6], D. A. Schwartz[7], E. S. Perlman[8], H. L. Marshall[9], M. Birkinshaw[7,10], D. M. Worrall[7,10], M. Georganopoulos[11], and D. W. Murphy[12]
[1] International Centre for Radio Astronomy Research, Curtin University, G.P.O. Box U1987, Perth, WA 6102, Australia; L.Godfrey@curtin.edu.au
[2] Research School of Astronomy and Astrophysics, Australian National University, Cotter Road, Weston, ACT 2611, Australia
[3] Australia Telescope National Facility, CSIRO, P.O. Box 76, Epping, NSW 2121, Australia
[4] CSIRO, Industrial Physics, P.O. Box 218, Lindfield, NSW 2070, Australia
[5] School of Mathematics and Physics, University of Tasmania, Tas 7001, Australia
[6] Department of Physics, Durham University, South Road, Durham DH1 3LE, UK
[7] Harvard-Smithsonian Center for Astrophysics, 60 Garden Street, Cambridge, MA 02138, USA
[8] Physics and Space Sciences Department, Florida Institute of Technology, 150 West University Boulevard, Melbourne, FL 32901, USA
[9] Kavli Institute for Astrophysics and Space Research, Massachusetts Institute of Technology, Cambridge, MA 02139, USA
[10] HH Wills Physics Laboratory, University of Bristol, Tyndall Avenue, Bristol BS8 1TL, UK
[11] Department of Physics, Joint Center for Astrophysics, University of Maryland–Baltimore County, 1000 Hilltop Circle, Baltimore, MD 21250, USA
[12] Jet Propulsion Laboratory, 4800 Oak Grove Drive, Pasadena, CA 91109, USA
Received 2011 December 23; accepted 2012 June 19; published 2012 August 7

ABSTRACT

We present a detailed study of the x-ray, optical, and radio emission from the jet, lobes, and core of the quasar PKS 2101−490 as revealed by new *Chandra*, *Hubble Space Telescope* (*HST*), and ATCA images. We extract the radio to x-ray spectral energy distributions from seven regions of the 13″ jet, and model the jet x-ray emission in terms of Doppler beamed inverse Compton scattering of the cosmic microwave background (IC/CMB) for a jet in a state of equipartition between particle and magnetic field energy densities. This model implies that the jet remains highly relativistic hundreds of kiloparsecs from the nucleus, with a bulk Lorentz factor $\Gamma \sim 6$ and magnetic field of the order of 30 μG. We detect an apparent radiative cooling break in the synchrotron spectrum of one of the jet knots, and are able to interpret this in terms of a standard one-zone continuous injection model, based on jet parameters derived from the IC/CMB model. However, we note apparent substructure in the bright optical knot in one of the *HST* bands. We confront the IC/CMB model with independent estimates of the jet power, and find that the IC/CMB model jet power is consistent with the independent estimates, provided that the minimum electron Lorentz factor $\gamma_{\rm min} \gtrsim 50$, and the knots are significantly longer than the jet width, as implied by de-projection of the observed knot lengths.

Key words: galaxies: active – galaxies: jets – quasars: individual (PKS 2101−490)

Online-only material: color figures

1. INTRODUCTION

The first *Chandra* observations of the quasar PKS 0637−752 revealed a bright x-ray jet extending 12″ from the quasar core (>500 kpc de-projected, assuming a jet viewing angle $\theta < 9°$, as evidence by the observed proper motions of the pc-scale jet using a modern cosmology; Lovell et al. 2000), associated with the previously known radio jet, but with an unexpectedly high x-ray to radio flux density ratio (Schwartz et al. 2000; Chartas et al. 2000). Since then, tens of quasar jets have been found to possess x-ray jets with similarly high x-ray to radio flux density ratios (e.g., Harris & Krawczynski 2002; Sambruna et al. 2002, 2004; Marshall et al. 2005, 2011; Kataoka & Stawarz 2005; Massaro et al. 2011). The strong x-ray emission from kiloparsec-scale quasar jets such as that of PKS 0637−752 is hard to explain in terms of standard emission mechanisms such as thermal bremsstrahlung or synchrotron self-Compton emission (Chartas et al. 2000; Schwartz et al. 2000). A popular explanation for the strong x-ray emission is the beamed, equipartition IC/CMB model proposed for PKS 0637−752 by Tavecchio et al. (2000) and Celotti et al. (2001), in which the flow velocity is assumed to be highly relativistic and directed close to the line of sight. A relativistic jet velocity increases the energy density of the cosmic microwave background (CMB) in the rest frame of the jet plasma, thereby increasing the x-ray emissivity produced via inverse Compton (IC) scattering of CMB photons. The small jet viewing angle implies that the emission is Doppler beamed toward the observer. The appeal of this model is largely due to its simplicity and consistency with equipartition between magnetic and particle energy densities in the emitting plasma. From here on, we refer to the beamed, equipartition IC/CMB model as simply the IC/CMB model.

A number of uncertainties and potential problems for the IC/CMB model have been identified: (1) there is no conclusive theoretical or empirical justification for the assumption of equipartition in jet plasma, although, for a given jet speed, the equipartition condition minimizes the plasma energy density and jet power. (2) The IC/CMB model requires jet Lorentz factors of the order of $\Gamma \sim 5$–25 on scales of hundreds of kiloparsecs from the core. Such large jet Lorentz factors are inconsistent with studies of the radio emission from large-scale jets and counter-jets ($\Gamma \lesssim 1.5$; Wardle & Aaron 1997; Mullin & Hardcastle 2009). A suggested solution to this problem invokes velocity structure across the jet—the so-called spine-sheath model, in which the radio emission from jets in FRII radio galaxies is dominated by a slower moving sheath, while the emission from quasar jets with small viewing angles is said to be dominated by the Doppler boosted radiation from a fast moving spine (see, e.g., Hardcastle 2006; Mullin & Hardcastle 2009). (3) It has been argued that, due to the long cooling timescale for the $\gamma \sim 100$ electrons responsible for the IC/CMB x-ray emission, radiative and adiabatic losses alone cannot account for the rapid drop in x-ray surface brightness outside the knots (Tavecchio et al. 2003; Stawarz et al. 2004; Siemiginowska

et al. 2007). (4) The IC/CMB model makes strong, testable predictions about the redshift dependence of kiloparsec-scale x-ray jets. Specifically, the model predicts that the x-ray surface brightness should be redshift independent, because the CMB energy density increases as $(1 + z)^4$ which balances the usual $(1 + z)^{-4}$ decrease of surface brightness with redshift. Therefore, the ratio of x-ray to radio surface brightness should be a strong function of redshift (Schwartz 2002; Marshall et al. 2011). So far, the search for the predicted redshift dependence has been unsuccessful (Marshall et al. 2011; Kataoka & Stawarz 2005). (5) It has been argued (e.g., Atoyan & Dermer 2004) that the very large jet powers derived from the IC/CMB model ($\gtrsim 10^{48}$ erg s^{-1}; e.g., Tavecchio et al. 2000) are prohibitively large. Such high jet power is disfavored because 10^{48} erg s^{-1} is equal to the Eddington luminosity of a 10^{10} $M_\odot$ black hole, and such high jet power is an outlier when compared to samples of FRII radio galaxies such as the Rawlings & Saunders (1991) sample, for which the largest estimated jet power is of the order of 10^{47} erg s^{-1}. (6) A number of sources show a decreasing x-ray to radio flux density ratio along the jet, which, if the IC/CMB model is correct, implies deceleration must be taking place on hundreds of kiloparsecs scales (Georganopoulos & Kazanas 2004). However, it is not clear how the gradual deceleration can occur, and there is no evidence for deceleration in lobe-dominated radio galaxies, which may be expected in such a model (Hardcastle 2006).

Despite the numerous concerns surrounding the IC/CMB model, none of the issues listed above is currently seen as definitively refuting the model, and it continues to receive attention in the literature as the likely candidate for the quasar jet x-ray emission mechanism. In this paper, we critically assess the application of the IC/CMB model to jet x-ray emission of PKS 2101−490.

PKS 2101−490 was first reported as a bright flat spectrum radio source by Ekers (1969). Marshall et al. (2005) reported a redshift of $z \approx 1.04$ for this source, based on an unpublished Magellan spectrum (see also the discussion in Section 6). The spectroscopic redshift determination is robust, with uncertainty of approximately ±0.003. Further details of the spectroscopic observations and data analysis will be presented in an upcoming paper (J. Gelbord & H. L. Marshall, in preparation).

Studies at the Australia Telescope Compact Array (ATCA) revealed significant radio emission on arcsecond scales (Lovell 1997). For this reason, PKS 2101−490 was included in the *Chandra* snapshot survey of flat spectrum radio quasars with arcsecond scale radio jets (Marshall et al. 2005). Marshall et al. (2005) presented an 8.6 GHz ATCA image along with a 5 ks snapshot *Chandra* image (Chandra ObsID 3126) that revealed significant x-ray emission associated with the 13″ eastern radio jet. Based on the results of the snapshot survey, and its morphological similarity to PKS 0637−752, PKS 2101−490 was selected along with a number of other sources: PKS 1421−490 (Godfrey et al. 2009; Gelbord et al. 2005), PKS 1055+201 (Schwartz et al. 2006b), PKS 0208−512 (Perlman et al. 2011), PKS 1202−262 (Perlman et al. 2011), PKS 0920−397 (Schwartz et al. 2010), and PKS 1030−357, as a target for deeper follow-up observations with *Chandra*, *Hubble Space Telescope* (*HST*), and ATCA. Here, we present a detailed physical analysis of the jet, hotspot, and lobes of this source based on new ATCA, *Chandra*, and *HST* follow-up images.

In Section 2, we describe the observations and data reduction. In Section 3, we discuss the method and results of modeling the spectral energy distributions of spatially separated jet knots in terms of the IC/CMB model. In Section 4, we compare independent jet power estimates with that obtained from the IC/CMB model of jet x-ray emission. In Section 5, we discuss the optical emission detected from one of the jet knots and present an interpretation of this in terms of a broken power-law synchrotron spectrum. In Section 6, we discuss the x-ray spectrum of the quasar core. In Section 7, we discuss the radio and x-ray emission from the lobes, in particular, we model the lobe SEDs in terms of IC scattering of the CMB. In Section 8, we present the conclusions and final remarks.

Table 1
Observation Information

Instrument	Band	Mode	Date
ATCA	4.8 GHz	1.5A/6A	2000 May 25/Sep 2
ATCA	8.64 GHz	1.5A/6A	2000 May 25/Sep 2
ATCA	17.73 GHz	6C	2004 May 10
ATCA	20.16 GHz	6C	2004 May 10
HST	F814W	ACS/WFC	2005 Mar 8
HST	F475W	ACS/WFC	2005 Mar 8
Chandra	0.5–7 keV	ACIS-S3	2004 Dec 17

2. OBSERVATIONS AND DATA REDUCTION

2.1. Overview

Figure 1 illustrates the radio structure of the source and the naming convention used for the various features in the radio maps. Figure 2 illustrates the polarization characteristics of the jet. We have extracted radio, optical, and x-ray flux densities from the seven major emission regions identified in Figure 1. In this section, we describe the observations in each waveband, as well as the methods used to measure flux densities and sizes for the individual jet knots. Table 1 lists the observational information for all data used in this study.

2.2. Radio

PKS 2101−490 was observed with the ATCA at 4.8 GHz and 8.64 GHz in two configurations, 1.5A and 6A, on 2000 May 25 and 2000 September 2, respectively, and in a single configuration (6C) at 17.7 GHz and 20.2 GHz on 2004 May 10. In each case, a full 12 hr synthesis was obtained, recording 128 MHz bandwidth in all four polarization products. Regular scans on the nearby phase calibrator PKS 2106−413 were scheduled throughout the observations, as well as scans on the ATCA flux calibrator PKS 1934−638. Standard calibration and editing procedures were carried out using the MIRIAD data analysis package. Following calibration, the data were exported to DIFMAP and several imaging/self-calibration iterations were performed. The data were both phase and amplitude self-calibrated.

2.2.1. Radio Knot Flux Density and Size Measurements

The spectrum of the entire jet (excluding lobe emission) between 4.8 GHz and 20.2 GHz is well described by a power law with spectral index $\alpha = 0.81 \pm 0.01$ (flux density $S_\nu \propto \nu^{-\alpha}$). Each of the four flux density measurements is within 1% of the best-fit power law (see Table 2), giving us confidence in the flux density and spectral index measurements for the entire jet. However, inspection of individual knot spectra indicates that the systematic uncertainties in flux density measurements for individual knots are significantly greater than the off-source rms. There are a number of factors contributing to the systematic uncertainty in the measurement of the relative strengths of individual knots, including the uniqueness problem that results

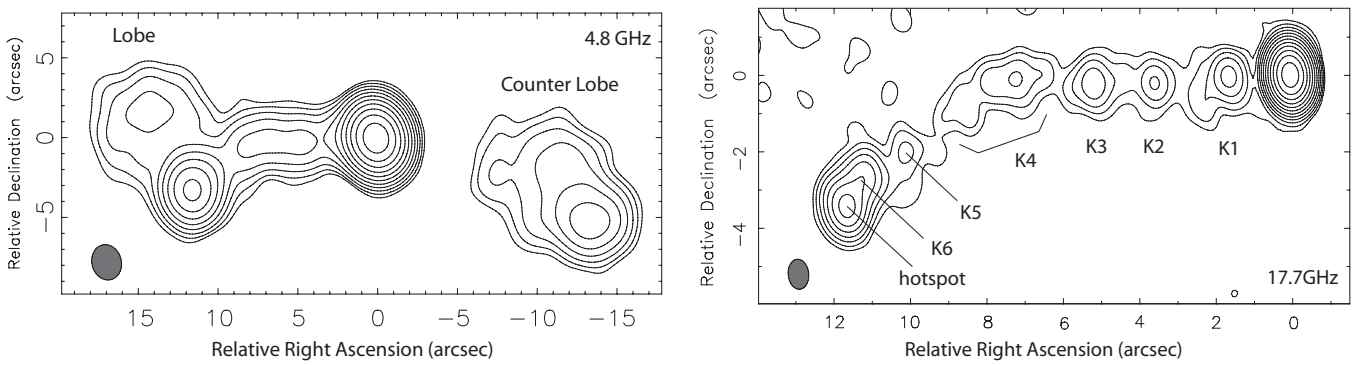

Figure 1. ATCA images at 4.8 GHz (left) and 17.7 GHz (right) showing the radio structure of the jet and lobes of PKS 2101−490. Also shown is the naming convention used for various components of the jet. The scale of this image is 8.1 kpc arcsec^{-1}. Contours are separated by a factor of two in surface brightness. In the 4.8 GHz image, the lowest contour is 0.42 mJy beam^{-1} and the beam FWHM is 2.″24 × 1.″84. In the 17.7 GHz image, the lowest contour is 0.15 mJy beam^{-1} and the beam FWHM is 0.″79 × 0.″54.

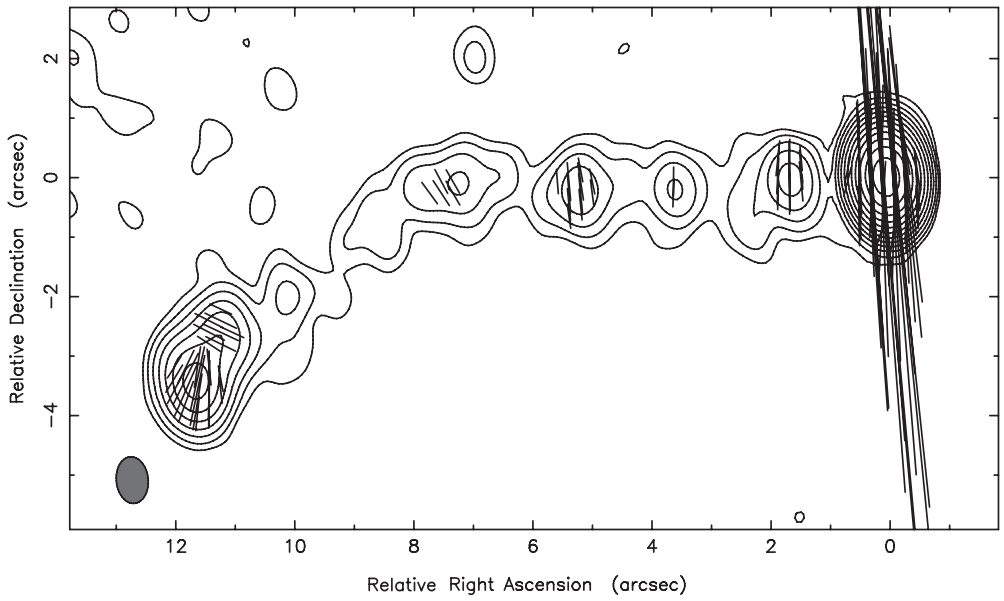

Figure 2. Same as Figure 1 (right) with polarization *E*-vectors overlaid. The *E*-vectors are scaled such that a length of 1 arcsec corresponds to 1 mJy beam^{-1} polarized surface brightness.

from gaps in the (u, v)-coverage due to the small number of telescopes (see, e.g., Walker 1995), and weak interknot emission that is detected at different levels in each band, as a result of the different (u, v)-coverage at each frequency. Also, some of the knots at 8.6 GHz are only marginally resolved, so that flux density measurements of individual knots become difficult. These issues and estimation of systematic uncertainty are discussed in detail in Godfrey (2009). We are therefore unable to determine accurately the spectral index for each individual knot, and are instead forced to assume that each knot has the same spectral index as that of the entire jet, which has been determined accurately.

Knot sizes for jet components K1–K4 were measured by fitting two-dimensional (2D) Gaussian models to jet knots in the 17.7 and 20.2 GHz maps, using the AIPS task JMFIT. Knot 6 and the hotspot are partially blended even at 20 GHz, and for this reason we determined their flux density and size at 17.7 and 20.2 GHz by fitting elliptical Gaussian models to these components in the (u, v)-plane, using the *modelfit* function of DIFMAP. The knot size estimates for all knots are based only on the measurements from the highest resolution maps (17.7 and 20.2 GHz). At 8.6 GHz, for knots 2, 3, and 4, flux densities were obtained by integrating the surface brightness within a region encompassing the knot emission. For knot 6 and the hotspot, the flux densities at 8.6 GHz were determined by fitting elliptical Gaussian models to these components in the (u, v)-plane. Due to the limited resolution at 8.6 GHz, we were unable to accurately determine the flux density for knots 1 and 5.

The size estimates from the 17.7 GHz and 20.2 GHz images were consistent for some knots. However, in some cases the knot dimensions differed by as much as a factor of two. This is another indication that image fidelity is questionable in the high-frequency maps, and systematic errors resulting from the deconvolution/self-calibration process are significant. The knot sizes listed in Table 2 are averages of the parameters determined from the 17.7 GHz and 20.2 GHz images. The uncertainties in knot size are taken to be half the difference between the 17.7 and 20.2 GHz measurements.

2.3. Hubble Space Telescope Optical Observations

PKS 2101−490 was observed with the Advanced Camera for Surveys (ACS) Wide Field Camera 1 (WFC1) on the *HST* in two filters ($F475W$ and $F814W$) on 2005 March 8. A total exposure time of 2.3 ks was obtained in each filter. A sub-pixel dithering pattern, with CR-SPLIT images at each of three

Table 2
Characteristics of Spatially Resolved Jet Knots and Lobes

Knot ID	Flux Densities							De-convolved Dimensions		
	$F_{4.8\,\mathrm{GHz}}$ (mJy)	$F_{8.6\,\mathrm{GHz}}$ (mJy)	$F_{17.7\,\mathrm{GHz}}$ (mJy)	$F_{20.2\,\mathrm{GHz}}$ (mJy)	$F_{806\,\mathrm{nm}}$ (nJy)	$F_{475\,\mathrm{nm}}$ (nJy)	$F_{1\,\mathrm{keV}}$ (nJy)	ϕ_{Maj}[a] (mas)	ϕ_{Min}[a] (mas)	Vol[b] (cm^3)
Core	720 ± 40	830 ± 40	500 ± 50	470 ± 50	2.32×10^5	1.59×10^5	87 ± 3	...	...	...
Knot 1	...	...	5.1 ± 0.5	4.7 ± 0.5	60 ± 10	30 ± 10	<0.2	400 ± 100	250 ± 10	3×10^{65}
Knot 2	...	4.6 ± 0.5	2.3 ± 0.2	2.2 ± 0.2	<30	<30	<0.15	400 ± 100	<150	1×10^{65}
Knot 3	...	5.1 ± 0.5	3.5 ± 0.3	2.8 ± 0.3	<30	<30	0.5 ± 0.15	550 ± 100	330 ± 100	7×10^{65}
Knot 4	...	9 ± 1	4.7 ± 0.5	4.2 ± 0.4	<50	<50	1.3 ± 0.3	2500 ± 500	300 ± 50	3×10^{66}
Knot 5	...	...	1.0 ± 0.2	0.8 ± 0.2	<30	<30	0.2 ± 0.1	400 ± 100	300 ± 100	4×10^{65}
Knot 6	...	11 ± 1	6.5 ± 0.6	6.3 ± 0.6	180 ± 10	90 ± 10	0.75 ± 0.2	600 ± 50	400 ± 20	1×10^{66}
hotspot	...	30 ± 3	16 ± 1.5	14 ± 1.5	<30	<30	<0.16	340 ± 30	240 ± 20	2×10^{65}
Entire jet	115 ± 1	71 ± 1	40 ± 0.5	36 ± 0.5	...	...	3.3 ± 0.4	...	...	...
Lobe	16 ± 2	8 ± 1	4.5 ± 0.4	4 ± 0.4	...	...	0.5 ± 0.2	8600	6500	3×10^{69}
Counter lobe	65 ± 6	33 ± 3	17 ± 2	14 ± 1	...	...	1.5 ± 0.2	12000	9400	9×10^{69}

Notes.
[a] These are the FWHM Gaussian knot sizes, based on Gaussian fits to the radio data (except in the case of the lobes). In the case of K6 and the hotspot, the Gaussian fit was performed in the (u, v)-plane (see Section 2.2.1). For all other jet knots, a Gaussian model was fit to the data in the image plane. In the case of the lobe and counter lobe, the quoted sizes are simply the size of the flux extraction regions—no fitting was done for the lobes.
[b] These are apparent (projected) volumes calculated assuming ellipsoidal geometry, i.e., $V = (\pi/6)\, D_{\mathrm{eq}}^2\, D_{\mathrm{pol}}$ where D_{eq} is the equatorial diameter and D_{pol} is the polar diameter of the ellipsoid. If the knots are associated with stationary features in the jet, the de-projected volumes will be greater by a factor of $(1/\sin\theta)$ where θ is the angle to the line of sight.

positions along a chip diagonal, was utilized to eliminate bad pixels and allow us to maximize the angular resolution, as the ACS/WFC does not fully sample the PSF at either 4750 or 8000 Å. An ORIENT was chosen such that the jet did not fall within 25° of a diffraction spike. The data were retrieved from the Multi-mission Archive at Space Telescope (MAST) Web site,[13] however, multiple peaks in the pipeline drizzled image of the quasar core suggested that a re-reduction of the data was required. In addition, the pipeline does not take into account sub-pixel dithering, which was performed in order to recover PSF information from the undersampling of the *HST* PSF. The re-reduction involved running MULTIDRIZZLE with a smaller PIXFRAC and scale, so that the images could be sub-sampled to 0.0247 arcsec pixels, and checking the alignment of the images with TWEAKSHIFTS. The best reference files indicated in the *HST* archive were used for the re-reduction. The position of the optical quasar core was aligned with the position of the radio core. This required shifting the optical data by approximately 0.″4.

We used TinyTIM simulations (Krist & Burrows 1994; Suchkov & Krist 1998; Krist & Hook 2004) to obtain sub-sampled PSF simulations for both bands. For those simulations, we assumed an optical spectrum of the form $F_\nu \propto \nu^{-1}$, although experience has shown that the PSF shape is not heavily dependent on spectral slope. Rotating the PSF to a north-up position for use with the drizzled images required independently rotating the two axes as the WFC detector's axes are not completely orthogonal on the sky. We normalized the PSF to the total number of counts in a 2″ circular aperture centered on the source. This takes advantage of the fact that charge "bleed" on the ACS is linear and charge is conserved for a saturated source (Gilliland 2004), and enables optimal matching of the PSF's outer portion to what is observed. Because the quasar core was saturated in the individual exposures, this inevitably led to negatives in the central pixels when PSF subtraction was done; however, given the small residuals in other places plus the smooth off-jet isophotes, we believe that the result is reliable. Subtraction of the PSF allowed us to look for optical jet components within 1″–2″ and resulted in a detection of Knot 1 in both bands.

Figure 3 shows the resulting optical maps with radio contours overlaid. In these images, the *HST* data have been smoothed with a 0.3 arcsec FWHM Gaussian to better show the optical emission from knot K6, which is clearly detected in both filters. It is interesting to note that the $F814W$ image of K6 reveals an elongated, double structure that is not apparent in the $F475W$ image of K6. We further note that the position of the optical emission from K6 is coincident with the radio position to within the uncertainties associated with the optical–radio image alignment. We consider the interpretation of the optical data in Section 5.

2.3.1. Optical Flux Density Measurements

Knots 1 and 6 are the only jet features detected in the optical images. Optical flux densities were measured using standard aperture photometry techniques. The appropriate aperture corrections were taken from Sirianni et al. (2005, Table 3), and the appropriate extinction corrections were taken from Sirianni et al. (2005, Table 14) assuming $E(B-V) = 0.039$ at the position of PKS 2101−490.[14] The optical flux densities and upper limits are given in Table 2.

2.3.2. The Extent of Optical Emission from Knot 6

We estimated the size of the optical emission from K6 as follows. First, the optical images were convolved with 0.″15 FWHM Gaussian. We then produced integrated profiles both parallel and perpendicular to the jet axis for the knot K6, a nearby star, and the TinyTim generated PSF using the ds9 projection capability. From the integrated profiles, we measured the FWHM of each[15] feature to be Θ_{K6}, Θ_{star}, and Θ_{PSF}. The

[13] *HST* archive http://archive.stsci.edu/.

[14] This value for $E(B-V)$ was obtained using the NASA Extragalactic Database extinction calculator http://nedwww.ipac.caltech.edu/forms/calculator.html, which is based on the Galactic reddening maps of Schlegel et al. (1998).

[15] The longitudinal profile in the $F814W$ band appears double peaked, so in that case, we estimated the extent of the optical emission region simply via inspection of the profile (Figure 4).

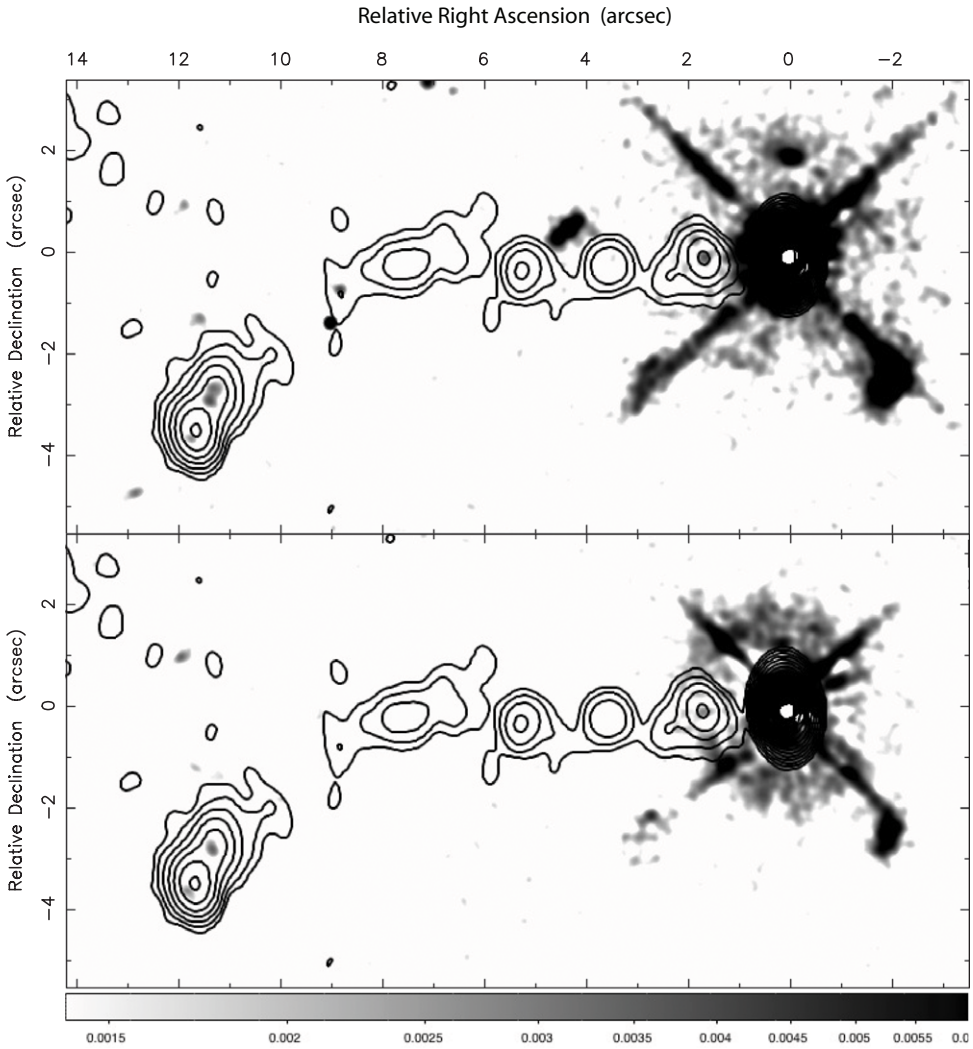

Figure 3. *HST* images of PKS 2101−490 (gray scales: top = $F814W$; bottom = $F475W$) with 20.2 GHz ATCA radio contours overlaid. The *HST* images have been sub-sampled with pixel size 0.″0247, PSF subtracted from the quasar core, and smoothed with a 0.″3 FWHM Gaussian to better show the optical counterpart to knot K6. The diffraction spikes are merely the residuals after PSF subtraction from the quasar core (see the text).

profiles of the star and TinyTim PSF are in good agreement with each other, and indicate that in the smoothed maps, the PSF FWHM is $\Theta_{\rm PSF} \approx \Theta_{\rm star} \approx 0.''18$ for both the $F475W$ and $F814W$ bands. We then calculated the de-convolved (intrinsic) extent of the optical emission associated with the knot K6 as $\Theta_{\rm K6,intrinsic} = \sqrt{\Theta^2_{\rm K6} - \Theta^2_{\rm PSF/Star}}$. The measured PSF sizes in the smoothed *HST* maps correspond to an un-smoothed PSF of 0.″11 in both bands, as expected for ACS/WFC. We note that the profile of K6 along the jet in the $F814W$ band appears double peaked, in contrast to the $F475W$ profile which is single peaked (see Figures 3 and 4).

The optical knot appears smaller than the associated radio knot; in both bands, the cross-jet width of the optical emission associated with K6 is significantly less than the measured width in the radio band (Table 3). The length of K6 parallel to the jet in the $F814W$ map appears marginally resolved, while the length of K6 in the $F814W$ map is clearly resolved, and appears to consist of two peaks (Figure 4). A discussion of the optical emission from K6 is presented in Section 5.

Table 3
Knot 6 (K6) De-convolved Sizes

Band	Cross-jet[a] (arcsec)	Along-jet[a] (arcsec)
ATCA 20.2 GHz	0.4 ± 0.02	0.6 ± 0.05
HST $F814W$	$0.24^{+0.03}_{-0.24}$	0.4 ± 0.1
HST $F475W$	$0.24^{+0.03}_{-0.24}$	$0.2^{+0.03}_{-0.2}$
Chandra 0.5–7 keV	<0.6	<0.6

Notes.
[a] These are the intrinsic FWHM Gaussian knot sizes, obtained via $\Theta_{\rm K6,intrinsic} = \sqrt{\Theta^2_{\rm K6} - \Theta^2_{\rm PSF}}$, except in the case of $F814W$ along-jet, which exhibits a double-peak structure. In that case, the extent of the emission region was estimated by inspection of the longitudinal knot profile (Figure 4).

2.4. Chandra X-ray Observations

PKS 2101−490 was observed with the *Chandra* x-ray observatory on 2004 December 17 (Cycle 6) using the Advanced CCD Imaging Spectrometer (ACIS-S) for a total exposure time of 42 ks (Chandra ObsID 5731). To reduce the effect of pile-up in the quasar core, a 1/4 subarray mode was used with a single CCD, so that the frame time was 0.8 s. The source was positioned close to the read-out edge of the CCD to reduce the effect of charge transfer inefficiency. A new Event 2 data file was made with pixel randomization removed, and the x-ray and radio core

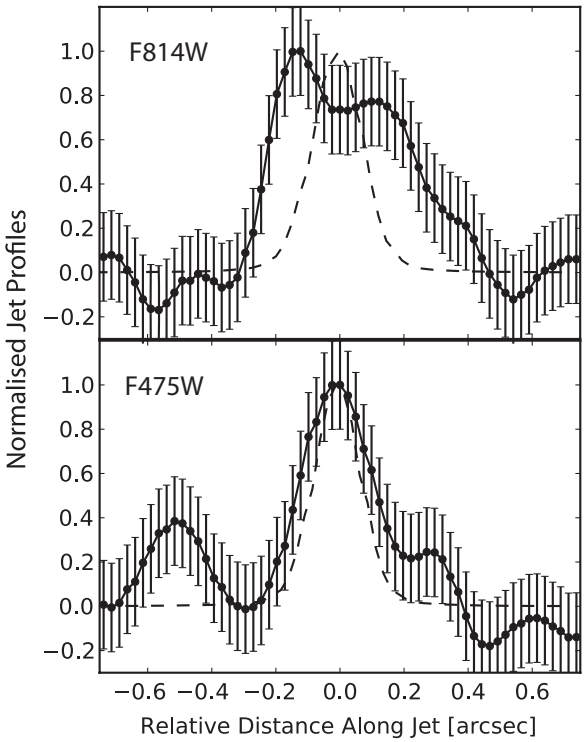

Figure 4. Longitudinal jet profiles of knot 6 in both *HST* bands along a position angle of 150°, integrated across a region of width 0.″5. These plots serve to illustrate the difference in the apparent knot length in each band, and the relative alignment of the peaks. Note that the peak in the *F*475*W* profile lies between the peaks in the *F*814*W* profile. The *HST* maps were smoothed by a Gaussian with 0.″15 FWHM before producing these profiles. The profile of the PSF, smoothed by a Gaussian with 0.″15 FWHM, is represented by the dashed curve in each plot. The error bars are based on the rms of profiles made in off-source regions.

positions were aligned, requiring a shift of the x-ray data by approximately 0.″4. The data were restricted to the energy range 0.5–7 keV.

2.4.1. X-ray Flux Density Measurements

The x-ray flux densities for individual knots were obtained by calculating the background-subtracted counts in each knot region and multiplying by the conversion factor. The conversion factor was estimated by fitting an absorbed power-law spectrum to the x-ray counts extracted from the whole jet. The x-ray spectra of the jet and lobe were fitted using the Sherpa software package by minimizing the Cash statistic (related to the log of the likelihood). The instrument response functions (RMF and ARF) were determined from the CALDB calibration database appropriate for the position of the source on the ACIS-S3 chip. In all model fits, the neutral hydrogen column density was fixed at the Galactic value 3.4×10^{20} cm^{-2} as determined from the COLDEN[16] column density calculator provided by the *Chandra* X-ray Center. The uncertainties for the flux density and spectral index were calculated using the "Covariance" routine in Sherpa. The results of this routine are valid provided that the surface of log likelihood is approximately shaped like a paraboloid. The "Interval-Projection" routine in Sherpa was used to verify that this condition was met.

We extracted a total of 138 counts from the jet having energies in the range 0.5–7.0 keV. Fitting a power law gives 1 keV flux density $S = 3.3 \pm 0.4$ nJy and spectral index $\alpha_X = 0.85 \pm 0.2$. This implies that the conversion factor is $G \approx 1.0$ μJy count^{-1} s^{-1} for a spectral index of $\alpha \approx 0.85$. In the counter lobe, we extracted a total of 55 counts in the energy range 0.5–7.0 keV. Following the same procedure as for the jet, we find flux density $S = 1.5 \pm 0.2$ nJy at 1 keV and spectral index $\alpha = 1.3 \pm 0.3$, implying the conversion factor is $G = 1.15$ μJy count^{-1} s^{-1} for a spectral index $\alpha \approx 1.3$. These estimates of the conversion factor are consistent with the predictions of the *Chandra* proposal planning toolkit.

Figure 5(A) is a comparison of x-ray and radio structure in the jet of PKS 2101−490 and Figure 5(B) illustrates the regions used to extract x-ray counts for the knots. The regions shown in Figure 5(B) (except for the hotspot extraction region—this region is discussed further below) have sides $\gtrsim$1.″6. Knots 5, 6, and the hotspot are difficult to separate in the *Chandra* image. In order to estimate the counts associated with the hotspot and avoid contamination from knot 6, a region encompassing only one side of the hotspot is used (the side furthest from knot 6). Due to the background in the vicinity of the hotspot and the possibility of contamination from knot 6, the few counts within this aperture may not be associated with the hotspot, and therefore the flux density estimate for the hotspot is an upper limit. An aperture correction of two is used when calculating the upper limit, since the flux extraction region encompasses only one side of the hotspot.

In the *Chandra* image, knot 1 is blended with the wings of the x-ray core. To place a limit on the x-ray flux density from knot 1, a sector of an annulus centered on the core was used, as shown in Figure 5(B). The background was estimated using the section of the annulus excluding knot 1. The data are consistent with zero counts from knot 1.

2.4.2. The Extent of X-ray Emission from Knot 6

The x-ray knot size is of great significance to models of jet x-ray emission (Tavecchio et al. 2003). Only knot 6 has sufficient counts and is sufficiently isolated from other strong knots to allow an accurate estimate of the knot size. Using the CIAO task *dmlist*, events were extracted from a 0.″8 radius circular aperture centered on knot 6. This region was chosen to be large enough to include a large fraction of the counts from knot 6, but small enough to avoid contamination from neighboring regions of the jet. Note that the encircled energy fraction within a circular aperture of radius 0.″8 is $\gtrsim$85% for a spectral index of $\alpha \sim 0.8$. A total of 29 events were extracted from this region. We assume, for simplicity, that the knot surface brightness profile and the inner 0.″8 of the *Chandra* PSF are both approximately Gaussian with variance $\sigma^2_{\rm K6}$ and $\sigma^2_{\rm PSF,\,0.''8}$ respectively. We estimated the variance ($\sigma^2_{\rm PSF,\,0.''8}$) of the *Chandra* PSF within a 0.″8 radius aperture by extracting events within a 0.″8 circular aperture centered on the core, and calculating the standard deviation of event coordinates. Doing so, we find $\sigma_{\rm PSF,\,0.''8} = 0.''29 \pm 0.''10$. This comparison between core and jet PSF is valid since the core and jet x-ray spectral indices are similar, and the core is not significantly affected by pile-up. We find that knot 6 is unresolved in both the jet and cross-jet directions.

To obtain an upper limit to the size of knot 6 we use the standard deviation distribution (Kenney & Keeping 1951). We find that the 99% upper limit to the x-ray knot size is $\sigma_{\rm obs,\,upper} = 0.''4$. The upper limit to the de-convolved (intrinsic) size of knot 6 (taken as the Gaussian FWHM) is then $D_{K6} < 2\sqrt{2\ln 2}(\sigma^2_{\rm obs,\,upper} - \sigma^2_{\rm PSF,\,0.''8})^{1/2} = 0.''6$ in both the jet and

[16] The COLDEN column density calculator, available at http://cxc.harvard.edu/toolkit/colden.jsp, based on Dickey & Lockman (1990).

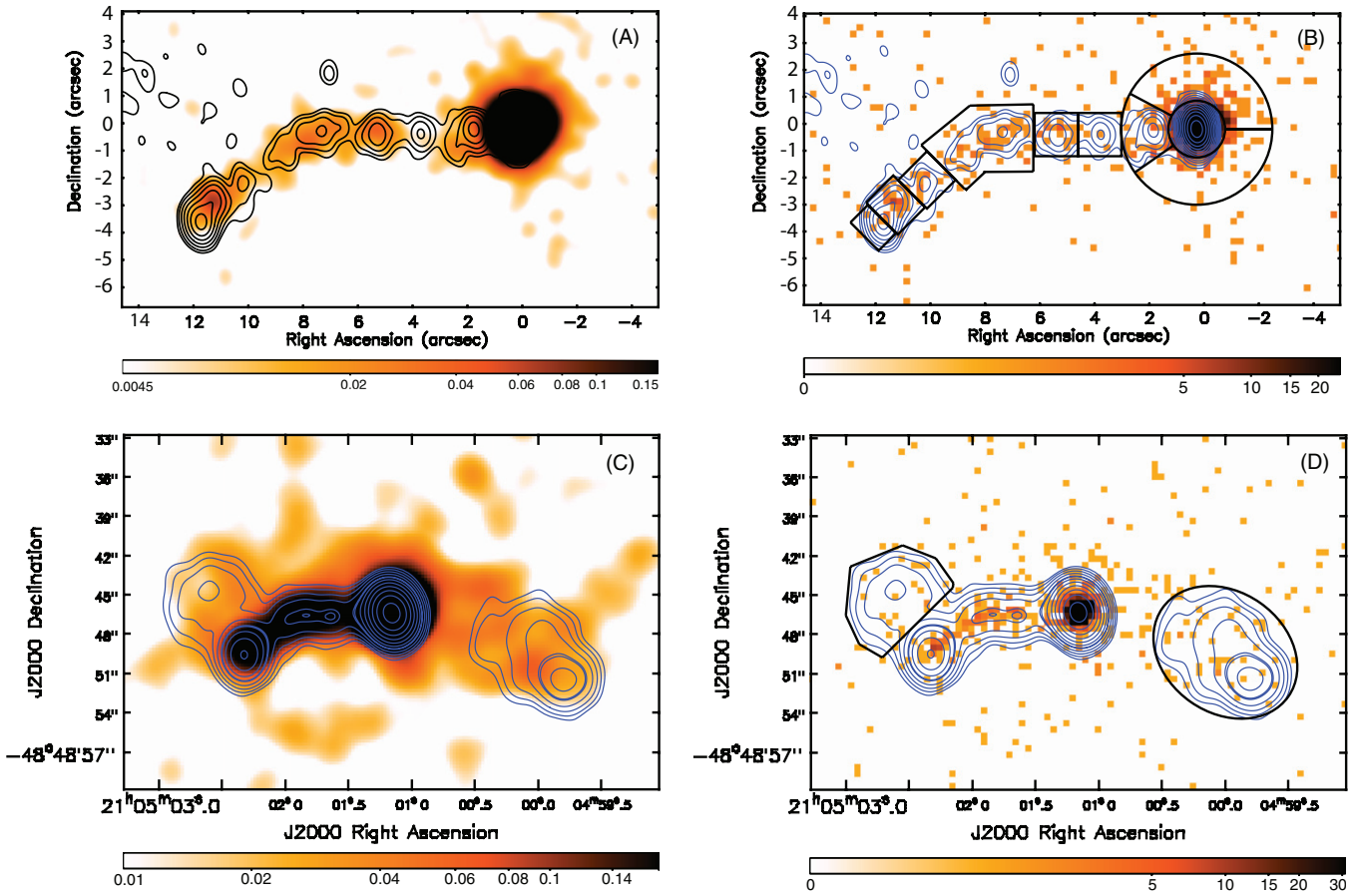

Figure 5. (A) X-ray image binned to 0.″0492 pixels and smoothed with a 0.″7 FWHM Gaussian with 17.7 GHz ATCA contours overlaid. Color scale is logarithmic between 0.0045 and 0.15 counts beam^{-1}. (B) Raw x-ray counts image binned to half a *Chandra* pixel width (0.″246) with 17.7 GHz radio contours overlaid. Color scale is logarithmic between 0 and 25 counts. The black outlines mark the flux extraction regions used for x-ray flux density calculations. (C) X-ray image binned to 0.″246 pixels and smoothed with 0.″7 FWHM Gaussian. Color scale is logarithmic between 0.01 and 0.18 counts beam^{-1}. Blue contours are from the 4.8 GHz ATCA image. (D) Raw x-ray counts image with 4.8 GHz radio contours overlaid. Color scale is logarithmic between 0 and 30 counts. The black outlines mark the flux extraction regions used to calculate x-ray flux densities associated with the lobes.

(A color version of this figure is available in the online journal.)

cross-jet directions. Thus, the extent of the x-ray knot emission is less than or equal to the extent of the radio emission of knot 6.

3. RESULTS

In this section, we present a comparison of the radio and x-ray images; we describe the methods used to model the radio to x-ray SEDs of individual knots; and we present the results of spectral modeling.

3.1. Radio/X-ray Longitudinal Jet Profiles

Figure 6 illustrates the radio and x-ray longitudinal jet profiles. The x-ray surface brightness is greatest near the end of the jet. This is in contrast to the trend that is seen in sources such as 3C273 (e.g., Marshall et al. 2001; Sambruna et al. 2001), 0827+243 (Jorstad & Marscher 2004), and 1127–145 (Siemiginowska et al. 2002, 2007), where the x-ray brightness peaks closer to the core and the brightness of the knots decreases with distance from the core (see Georganopoulos & Kazanas 2004, for a discussion of this phenomenon).

3.2. Modeling the Spectral Energy Distributions of Spatially Separated Knots

The spectral energy distributions of the jet knots are typical of quasar x-ray jet knots such as those in PKS 0637−752: a single or broken power law is unable to fit the entire radio to x-ray SED, so that two spectral components are required to model the data (see Figure 7). The x-ray spectral index of the entire jet $\alpha_{0.5\ \mathrm{keV}}^{7.0\ \mathrm{keV}} = 0.85 \pm 0.2$ is consistent with the radio spectral index of the entire jet $\alpha_R = 0.81 \pm 0.01$. The data are therefore consistent with an IC interpretation for the x-ray emission.

3.2.1. Synchrotron Self-Compton Model

As with other quasar x-ray jets (e.g., Schwartz et al. 2000), synchrotron self-Compton (SSC) models for the x-ray jet emission in PKS2101−490 require sub-equipartition magnetic field strengths. The magnetic field strengths in the knots derived from SSC modeling are a factor of ∼50 below the equipartition (minimum energy) values (Godfrey 2009). Such sub-equipartition magnetic fields are generally disfavored, because in that case, the internal energy, internal pressure, and jet power (for a fixed jet speed) are orders of magnitude greater than in the case of equipartition magnetic fields. We note that if the jet is Doppler beamed, then the ratio of the equipartition magnetic field strength to the SSC-derived magnetic field strength increases approximately in proportion to $\delta^{2/(1+\alpha)}$.

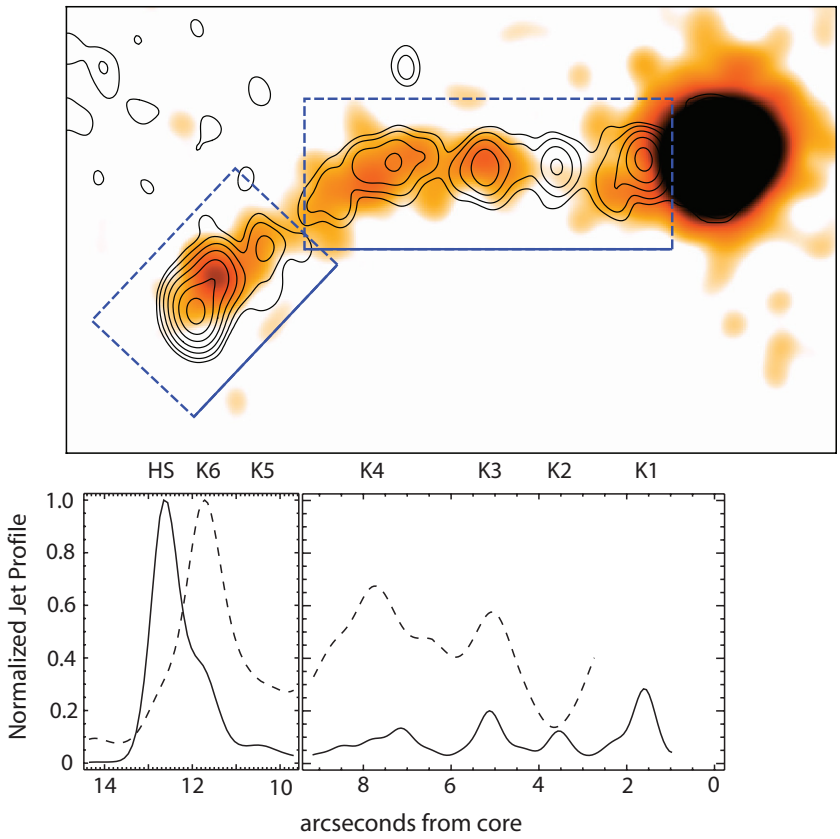

Figure 6. Top: x-ray image binned with 1/10 *Chandra* pixel width (0.″0492) and smoothed with a 0.″7 FWHM Gaussian to emphasize the x-ray jet structure. 17.7 GHz ATCA contours are overlaid. Also shown are the projection regions used to obtain the radio and x-ray jet profiles. Bottom: x-ray (dashed line) and radio (solid line) longitudinal jet profiles. These curves show the jet brightness integrated across the jet as a function of distance from the core along the jet ridge line. Note that in this plot, the x-ray resolution (1.″1) and radio resolution (0.″65) are not equal. These profiles simply serve to illustrate the differences in jet structure at each wavelength.

(A color version of this figure is available in the online journal.)

3.2.2. IC/CMB Modeling

In this section, we model the knot x-ray emission in terms of IC scattering of CMB photons in a highly relativistic jet directed close to the line of sight (Tavecchio et al. 2000; Celotti et al. 2001).

Assumed form of the electron energy distribution: in order to apply the analytic one-zone IC/CMB model (Dermer 1995; Harris & Krawczynski 2002; Worrall 2009), we assume a single power-law electron energy distribution $N(\gamma) = K_e\gamma^{-a}$ between a minimum and a maximum Lorentz factor, $\gamma_{\rm min}$ and $\gamma_{\rm max}$, with $a = 2.6$ (corresponding to synchrotron spectral index, $\alpha = 0.8$). We assume $\gamma_{\rm max} = 10^5$ for all knots. The assumed value for $\gamma_{\rm max}$ allows the synchrotron spectrum to cutoff at a frequency below that of the *HST* observing frequencies. The value of the high energy cutoff is not well constrained, however, the conclusions drawn from this model are not sensitive to the assumed value of $\gamma_{\rm max}$ (see Schwartz et al. 2006a, Appendix A). In contrast to the single power-law electron energy distribution assumed here, in Section 5 we model the synchrotron spectrum of Knot 6 in terms of a broken power law. We note that the results of the IC/CMB model are insensitive to the details of the high-energy end of the electron energy distribution, provided the break in the distribution occurs at $\gamma_{\rm break} \gg \gamma_{\rm min}$. Therefore, the assumption of a single power-law distribution in this section does not affect the conclusions drawn from this model for Knot 6, nor does it alter the conclusions drawn in later sections.

The low energy cutoff, $\gamma_{\rm min}$, is constrained so that the model does not produce optical IC/CMB emission above the *HST* upper limits or detections. This constraint on $\gamma_{\rm min}$ is possible because an extrapolation of the IC/CMB spectrum from x-ray to optical frequencies lies above the optical upper limits, and in the case of Knot 6, is comparable to the detection level but with an incorrect spectral index. In addition to this constraint, $\gamma_{\rm min}$ must not be so high that there is no significant x-ray emission produced at 0.5 keV. As we show in the following sections, the IC/CMB model requires a Doppler factor $\delta \sim 6$ at least in some parts of the jet. Assuming $\nu_{\rm min}^{\rm ic/cmb} \approx 1.6\times10^{11}\times\delta^2\gamma_{\rm min}^2$ Hz (see, e.g., Worrall 2009), we are able to constrain the value for $\gamma_{\rm min}$ to lie in the approximate range $10 \lesssim \gamma_{\rm min} \lesssim 200$. Mueller & Schwartz (2009) find marginal evidence for a value $\gamma_{\rm min} \approx 50$ in the jet of PKS 0637−752 based on spectral fitting of the jet x-ray spectrum. We therefore adopt $\gamma_{\rm min} = 50$ in the following analysis.

The model and assumptions: we use the standard one-zone IC/CMB model equations (see Worrall 2009) assuming a continuous jet geometry (i.e., $S_\nu \propto \delta^{2+\alpha}$ for the synchrotron flux density). Many of the jet knots appear elongated along the jet axis. Therefore, since this model requires the jet viewing angle to be small, we take into account projection effects in the calculation of knot volumes. Without independent constraints on the jet viewing angle, we simply assume a representative value in order to make an approximate de-projection. As we show in the following sections, the IC/CMB model requires a Doppler factor of the order of $\delta \gtrsim 6$ at least in some parts of the jet. This implies that the jet viewing angle must be $\lesssim 9^\circ$. Angles significantly less than 9° are unfavorable since that would imply

Table 4
IC/CMB Modeling Results

Knot ID	$\frac{F_{1\mathrm{keV}}}{F_{17.7\,\mathrm{GHz}}}$ ($\times 10^{-8}$)	δ	B_{eq} (μG)	n_e ($\times 10^{-6}$ cm^{-3})	$L_{\mathrm{jet}}^{e^-e^+}$ ($\times 10^{46}$ erg s^{-1})	$L_{\mathrm{jet}}^{e^-p}$ ($\times 10^{46}$ erg s^{-1})
Knot 1	<4	<6	>40	>0.6	<0.5	<3
Knot 2	<6.5	<7	>40	>0.5	<0.2	<1
Knot 3	14 ± 4	7	30	0.2	0.5	3
Knot 4	28 ± 7	7	20	0.1	0.2	1
Knot 5	20 ± 10	7	20	0.2	0.3	1
Knot 6	11 ± 3	6	30	0.3	0.7	4

Notes. Assumed model parameters: $\gamma_{\mathrm{min}} = 50$, $\gamma_{\mathrm{max}} = 10^5$, $\alpha = 0.8$, jet viewing angle $= 9^\circ$ (for de-projection of knot volumes given in Table 2), ratio of proton-to-electron energy densities (ϵ_p/ϵ_e) $\ll 1$. To calculate jet powers, we have assumed $\Gamma = \delta$.

uncomfortably large source size. For example, if the jet lies closer than 5° to the line of sight, then the total source size must be >2.3 Mpc. Therefore, we assume a jet viewing angle of $\theta = 9^\circ$ in making an approximate de-projection of the knot length along the jet axis, and note that this angle corresponds approximately to the maximum jet viewing angle given the derived Doppler factor $\delta \gtrsim 6$. The de-projected volumes, V, are related to the projected volumes V_0 as $V = V_0/\sin\theta$. The projected volumes V_0 are listed in Table 2. For the purposes of the current calculations, and to reduce the number of model parameters, we further assume that the proton contribution to the particle energy density is negligible.

The results of IC/CMB modeling are presented in Table 4. Included in the table is the jet kinetic energy flux, which we calculate based on the derived jet parameters in the case of purely leptonic and electron/proton jets, using Equation (B17) of Appendix B in Schwartz et al. (2006a), with the following simplifying assumptions: the bulk Lorentz factor of the jet $\Gamma \gg 1$, equipartition between particle and magnetic field energy densities, and a tangled magnetic field geometry such that $\langle B_\perp'^2 \rangle = (2/3)B^2$. With these assumptions, the expression for kinetic luminosity in the case of a purely leptonic and electron/proton jet, respectively, are (in cgs units)

$$L_{\mathrm{jet}}^{e^{+/-}} \approx \pi R^2 \Gamma^2 c \left(\frac{B^2}{3\pi}\right) \mathrm{erg\,s^{-1}}$$

$$L_{\mathrm{jet}}^{e^-p} \approx \pi R^2 \Gamma^2 c \left(\left(\frac{\Gamma - 1}{\Gamma}\right) n_e m_p c^2 + \frac{B^2}{3\pi}\right) \mathrm{erg\,s^{-1}}.$$

In the case of an electron/proton jet, we assume one cold proton for each relativistic electron. The electron density, n_e, in cgs units, is calculated from the spectral fits as

$$n_e \approx \frac{B^2}{8\pi m_e c^2} \left(\frac{a-2}{a-1}\right) \gamma_{\mathrm{min}}^{-1}, \quad (1)$$

where the magnetic field strength B is in Gauss.

The model-dependent results presented in Table 4 suggest that if the results of this model are correct, while the jet Lorentz factor remains approximately constant along the jet, the magnetic field and particle density decrease by a factor of a few between the innermost knots and the outer knots. The results indicate that there is modest, if any, loss of kinetic luminosity along the jet.

3.3. Comparison of Jet Morphology with PKS 0637−752 and PKS 0920−397

The jet of PKS 2101−490 undergoes an apparent bend of approximately 45° at about half way between the core and jet termination, somewhat reminiscent of the jet morphology in PKS 0637−752 (Schwartz et al. 2000). However, unlike PKS 0637−752, the x-ray emission in PKS 2101−490 is detected after the jet bend. This is of interest because a change in the jet viewing angle produces a change in the Doppler factor, which should manifest itself as change in knot brightness and the x-ray to radio flux density ratio. However, there is not a unique relationship between apparent bend angle and change in jet viewing angle. Therefore, the fact that x-ray emission continues beyond the bend in 2101–490 cannot be used to constrain the emission mechanism. It may simply be the case that the bend in 0637–752 is associated with a significant increase in the viewing angle (and hence a significant decrease in the Doppler factor), while the bend in 2101–490 may be associated with a relatively small change, or a decrease in viewing angle (and hence a small change or increase in the Doppler factor). Having said that, on a population basis, the probability distribution of change in the jet viewing angle for a given apparent bend angle may enable a useful constraint on the emission mechanism.

In addition to the morphological similarities to PKS 0637−752, we note a striking similarity between PKS 2101−490 and PKS 0920−397 (Schwartz et al. 2010), particularly in the vicinity of the jet termination. In both these sources, a bright, compact knot approximately 1 arcsec (>10 kpc deprojected) upstream from the jet termination is detected in radio, optical, and x-ray bands. A similar, x-ray bright pre-hotspot jet knot is seen in 1354+195 (Sambruna et al. 2002). One possible interpretation is that these pre-hotspot jet knots may be associated with an oblique shock that is produced as the jet enters the highly turbulent region at the head of the cocoon. Numerical simulations of extragalactic jets show that as the jet approaches the hotspot, it encounters an increasingly violent environment, with strong turbulence that can perturb the jet flow, inducing instabilities or directly causing oblique shocks to form due to density/pressure gradients in the lobes (e.g., Norman 1996). The pre-hotspot jet knots may be the result of the jet entering an increasingly violent environment near the hotspot.

4. COMPARING INDEPENDENT ESTIMATES OF JET ENERGY FLUX FOR PKS 2101−490

In this section, as a means to assess the validity of the IC/CMB model, our goal is to obtain independent estimates of jet power and compare these with the estimate of jet power derived from the IC/CMB model.

4.1. Jet Energy Flux from Hotspot Parameters

It is possible to estimate the jet power based on observed hotspot properties by applying the conservation of momentum and making a number of reasonable assumptions about the hotspot. In the following section, we carry out this approach and compare the hotspot-derived jet power estimates to those obtained from IC/CMB modeling of Knot 6—the jet feature closest to the hotspot.

Consider a uniform jet of area A, particle energy density ϵ, pressure p, mass density ρ, relativistic enthalpy $w = \epsilon + p + \rho c^2$, magnetic field perpendicular to the flow direction $B_\perp$ (as indicated by the polarization), speed $c\beta$, and the corresponding bulk Lorentz factor Γ. The kinetic power ($L_{\rm jet}$) and momentum flux (F_M) along the jet are, in c.g.s. units (e.g., Double et al. 2004):

$$L_{\rm jet} = A\Gamma^2\beta c\left(w + \frac{B_\perp^2}{4\pi}\right) \quad (2)$$

$$F_M = A\left[\Gamma^2\beta^2\left(w + \frac{B_\perp^2}{4\pi}\right) + p + \frac{B_\perp^2}{8\pi}\right]. \quad (3)$$

Let us first consider the region of the jet upstream of the hotspot. In this region, the IC/CMB model indicates that the jet Lorentz factor, $\Gamma \gg 1$. In such a highly relativistic jet, the kinetic power $L_{\rm E,jet}$ is simply related to the momentum flux $F_{\rm M,jet}$ via

$$L_{\rm jet} \approx c \times F_{\rm M,jet}. \quad (4)$$

We assume a near normal shock at the jet terminus and appeal to conservation of momentum, so that $F_{\rm M,jet} = F_{\rm M,hotspot}$, and thus $L_{\rm jet} \approx cF_{\rm M,hotspot}$. Assuming that the jet plasma in the hotspot is decelerated to a low velocity so that $\Gamma^2\beta^2 \ll 1$, the following relation then holds:

$$L_{\rm jet} \approx cA \times \left[p + \frac{B_\perp^2}{8\pi}\right]_{\rm hs}. \quad (5)$$

The above equality holds regardless of assumptions about the jet characteristics such as its composition or the ratio of magnetic to particle energy densities in the jet or hotspot. We estimate the jet kinetic luminosity simply by estimating the hotspot parameters. This technique of jet energy flux estimation will be considered further in an upcoming paper (L. E. H. Godfrey & S. S. Shabala, in preparation).

In order to estimate hot spot parameters, we assume that the lepton population is ultra-relativistic ($p = \epsilon/3$) and dominates the particle pressure. Then,

$$L_{\rm jet} \approx Ac\frac{B^2}{8\pi}\left(1 + \frac{1}{3}\frac{\epsilon_{e^\pm}}{\epsilon_B}\right). \quad (6)$$

As a check on this analysis, we apply it to the case of Cygnus A. Synchrotron self-Compton modeling of Cygnus A hotspot A, assuming a power-law electron energy distribution of the form $N(\gamma) = K_e\gamma^{-a}$, indicates $B = 150$ μG and $B_{\rm eq} = 280$ μG assuming $R = 2$ kpc and $a = 2.1$ (Wilson et al. 2000). For hotspot D, $B = 150$ μG and $B_{\rm eq} = 250$ μG assuming $R = 2.2$ kpc and $a = 2.05$. Wilson et al. (2000) do not give an estimate of the electron energy density, so we estimate the electron energy density from the SSC and equipartition magnetic field strengths as $\epsilon_e = (B_{\rm eq}^2/8\pi)(B/B_{\rm eq})^{(a+1)/2}$, since $\epsilon_e \propto K_e$ and the synchrotron flux density $S_\nu \propto K_e B^{(a+1)/2} \Rightarrow \epsilon_e \propto B^{-(a+1)/2}$, in the case of a power-law distribution of the form $N(\gamma) = K_e\gamma^{-a}$. Therefore, $\epsilon_e = 8 \times 10^{-9}$ erg cm^{-3} and $\epsilon_e = 5.4 \times 10^{-9}$ erg cm^{-3} for hotspots A and D, respectively. Hence, we find $L_{\rm jet} \approx 1 \times 10^{46}$ erg s^{-1} for both hotspots A and D. This estimate of the jet power in Cygnus A is in excellent agreement with the value obtained by Wilson et al. (2006), $L_{\rm jet} \gtrsim 1.2 \times 10^{46}$ erg s^{-1}, based on modeling the cocoon dynamics. An independent estimate of jet power in Cygnus A comes from Lobanov (1998), who show that frequency-dependent shifts of the radio core enable a determination of the jet parameters, which, when applied to the case of Cygnus A, gives a value for the jet power $L_{\rm jet} = (0.55 \pm 0.05) \times 10^{46}$ ergs s^{-1}.

We now return to the case of PKS 2101−490. The *Chandra* x-ray image provides only an upper limit to the hotspot x-ray flux density. Therefore, to calculate the hotspot magnetic field strength and particle energy density, we adopt equipartition estimates. We note that the adoption of an equipartition magnetic field strength does not overproduce hotspot x-ray emission, for which we have obtained an upper limit. We justify the assumption of equipartition by the fact that high-luminosity hotspots typically exhibit x-ray flux density consistent with the equipartition synchrotron self-Compton model predictions (Hardcastle et al. 2004). Moreover, the total energy density, and hence the derived jet power, is only weakly dependent on magnetic field strength for magnetic fields near equipartition conditions, so that moderate departure from equipartition does not alter our conclusions. For example, if the hotspot magnetic field strength were 1/3 the equipartition value, then our equipartition jet power would underestimate the true value by less than a factor of two.

The hotspot synchrotron spectral index is not well constrained, so we apply a single power-law model along with the following assumptions: $10 < \gamma_{\rm min} < 1000$, $\gamma_{\rm max} > 10^4$, $\alpha = 0.8$. This model, combined with the flux densities and volume listed in Table 2, indicates that $B_{\rm eq,hs} \sim 200$–450 μG. Due to the prior assumption of equipartition, we have $\epsilon_{e^\pm} = \epsilon_{\rm B}$. Taking $A = (6 \pm 1) \times 10^{43}$ cm^2 as estimated from the 20 GHz ATCA image, the jet energy flux calculated from the hotspot model is

$$L_{\rm jet} = (0.4\text{–}2) \times 10^{46}\,{\rm erg\,s^{-1}}. \quad (7)$$

The range of values reflects the range of $\gamma_{\rm min}$ assumed in the hotspot model, with the lower jet power corresponding to higher assumed values of $\gamma_{\rm min}$. Minimum Lorentz factors $\gamma_{\rm min} \approx 600$ have been observed in a number of hotspots (Godfrey et al. 2009 and references therein). This is an order of magnitude greater than the value of $\gamma_{\rm min}$ assumed in the jet. As suggested by Godfrey et al. (2009), such an increase in $\gamma_{\rm min}$ between the jet and hotspot may be due to the dissipation of jet energy in a relativistic proton/electron jet terminating at a near-normal shock.

4.2. Willott et al. $Q_{\rm jet}$–L_{151} Relation

A widely used method for estimating jet power in high-luminosity radio sources is based on the model of Willott et al. (1999), in which the jet power is estimated using the 151 MHz radio luminosity as follows:

$$Q_W \approx f^{3/2}1.5 \times 10^{38}\left(\frac{S_{151}D_L^2}{10^{28}\,{\rm W\,Hz^{-1}\,sr^{-1}}}\right)^{6/7}\ {\rm W}, \quad (8)$$

where Q_W is the kinetic power per jet, S_{151} is the flux density of the entire source at 151 MHz, D_L is the luminosity distance,

Table 5
Jet Power Derived from IC/CMB Modeling of K6 SED

Composition	$\gamma_{\rm min} = 10$	$\gamma_{\rm min} = 50$
Leptonic	1×10^{46} erg s^{-1}	7×10^{45} erg s^{-1}
Electron/proton	3×10^{47} erg s^{-1}	4×10^{46} erg s^{-1}

and f is a parameter that accounts for uncertainties in various model assumptions, with $1 < f \lesssim 20$ (see Willott et al. 1999, for details of the model). For high power sources, the value of f has not been constrained empirically, but is typically taken to be $f = 10$–20 (e.g., Fernandes et al. 2011; Hardcastle et al. 2007). We extrapolate flux density measurements of $S_{408\,\rm MHz} = 2.34$ Jy (Large et al. 1981), $S_{843\,\rm MHz} = 1.48$ Jy (Mauch et al. 2003), and $S_{1.41\,\rm GHz} = 1.1$ Jy (Wright & Otrupcek 1990) to estimate the flux density at 151 MHz—$S_{151\,\rm MHz} \approx 4.25$ Jy—and thereby obtain $Q_W \sim 1(3) \times 10^{46}$ erg s^{-1} assuming $f = 10(20)$.

4.3. Average Jet Power from Lobe Parameters and Source Age

Here, we estimate the average jet power over the life of the source based on the lobe parameters and an estimate of the source age

$$L_{\rm jet} \approx \frac{2U_{\rm lobe}}{t_{\rm age}}, \quad (9)$$

where $U_{\rm lobe}$ is the total (magnetic plus particle) energy contained in the lobe. The factor of two is an approximate correction accounting for the fraction of jet energy converted to lobe kinetic energy and work done by the expanding lobes (Willott et al. 1999; Bicknell et al. 1997). In Section 7, we estimate the lobe parameters via synchrotron and IC modeling of the radio to x-ray SED, and argue that the source age is likely $t_{\rm age} \sim 10^8$ yr. Based on the results of Section 7, we estimate the average jet power over the life of the source to be $L_{\rm jet} \gtrsim 10^{45}$ erg s^{-1}. This is a factor of 4–20 lower than the other estimates of jet power. We note that we have ignored the possible contribution of protons to the energy density of the lobes, and we have ignored adiabatic cooling in estimating the cooling rate in the above analysis, each of which would increase the jet power estimate. We note that the calculations in Section 7 involve projected volumes. Using de-projected volumes will not increase the total energy, since the product $K_e \times V$ remains constant and the particle energy dominates $U_{\rm lobe}$ in this source.

4.4. Discussion of the Results

Three independent order-of-magnitude estimates of jet power indicate $L_{\rm jet} \sim 10^{45}$–10^{46} erg s^{-1}. For comparison, the jet power obtained from the one-zone IC/CMB model of jet x-ray emission are given in Table 5, for different values of the minimum Lorentz factor $\gamma_{\rm min}$, and different assumed jet compositions.

It can be seen that, in the case of a purely leptonic composition, there is good agreement between the IC/CMB model and independent estimates of jet power, regardless of the value for $\gamma_{\rm min}$ within the stated limits. Under the assumption of a cold proton/electron composition, there is good agreement between the IC/CMB model and independent estimates of jet power, provided $\gamma_{\rm min} \gtrsim 50$. This assumes one cold proton per radiating electron. If relativistic protons are included, the lower limit on $\gamma_{\rm min}$ would increase.

We have shown that in the case of PKS 2101−490, the IC/CMB predicted jet power is $\ll 10^{48}$ erg s^{-1} (the "uncomfortably large" jet power derived for some quasar x-ray jets based on the IC/CMB model; Atoyan & Dermer 2004; Mehta et al. 2009) under a range of reasonable assumptions. Indeed, the IC/CMB derived jet power is comparable to independent estimates of $L_j \sim 10^{45}$–10^{46} erg s^{-1} for both leptonic and electron/cold proton compositions, provided $\gamma_{\rm min} \gtrsim 50$. An important point to note about our jet power estimates is that, for the IC/CMB model, we have used a cylindrical geometry for knot K6 with a length approximately 10 times its width. This highly elongated cylindrical geometry is required by the observation that knot K6 is elongated along the jet axis in the radio maps, and the fact that the jet must be aligned within $\lesssim 9^\circ$ of the line of sight if the IC/CMB model is to be applied. Typically, jet knots are assumed to be spherical with the knot diameters equal to the jet widths (e.g., Tavecchio et al. 2000; Mehta et al. 2009). If we were to assume a spherical volume in our analysis, then the IC/CMB derived jet powers would be greater by a factor of ∼4.

5. THE OPTICAL EMISSION FROM KNOT 6

5.1. Introduction

The rate of optical jet discovery[17] in objects with confirmed radio and x-ray jets is approximately two out of three. However, few of these sources have resolved optical knots, particularly at high redshift (excepting PKS 0637−752 in which multiple optical knots are resolved; Schwartz et al. 2000; Mehta et al. 2009), and while a systematic study has not yet been performed, it would appear that relatively few have detailed information regarding the spectral slopes in both the radio and optical bands.

In PKS 2101−490, knot 6 is the only jet region that is reliably detected in all three bands (radio, optical, and x-ray). The radio through optical spectrum for knot 6 can be fit using a broken power law with a break of $\Delta\alpha = 0.5$ (Figure 7). This suggests that radiative cooling may be responsible for the steeper spectrum at optical frequencies. However, the interpretation of the optical emission from Knot 6 is complicated by the fact that the optical to x-ray spectral index is $\alpha^{1\,\rm keV}_{6.32\times10^{14}\,\rm Hz} \approx 0.8$, consistent with the observed radio and x-ray spectral index of the entire jet. It is therefore plausible that a significant fraction of the observed optical flux density is IC/CMB emission. For the IC/CMB model to produce the observed optical flux at 6.32×10^{14} Hz, the electron energy distribution must continue with the same slope to Lorentz factors $\gamma \lesssim 10$, assuming $\Gamma \sim \delta = 6$. If the electron distribution cuts off at a Lorentz factor $\gamma \gg 10$, the IC/CMB emission will not make a significant contribution to the observed optical flux density.

With this caveat in mind, in this section, we model the radio through optical spectrum in terms of a broken power-law synchrotron model, and consider whether the jet parameters derived from IC/CMB modeling are consistent with this interpretation of the radio to optical spectrum of knot 6. Figure 8 illustrates the broken power-law fit to the SED of knot 6. The parameters of this fit are $\alpha = 0.8$, $\nu_{\rm b} = 7 \times 10^{12}$ Hz and $\nu_{\rm max} = 10^{16}$ Hz.

5.2. Synchrotron Model for the Radio to Optical Spectrum of Knot 6

In modeling the radio to optical spectrum, we consider the effects of synchrotron cooling (Meisenheimer et al. 1989) and adopt the following procedure: we assume that relativistic electrons are injected at a shock with an energy index a (number

[17] See http://astro.fit.edu/jets/ for a listing of known optical/IR jet sources, and information for each source.

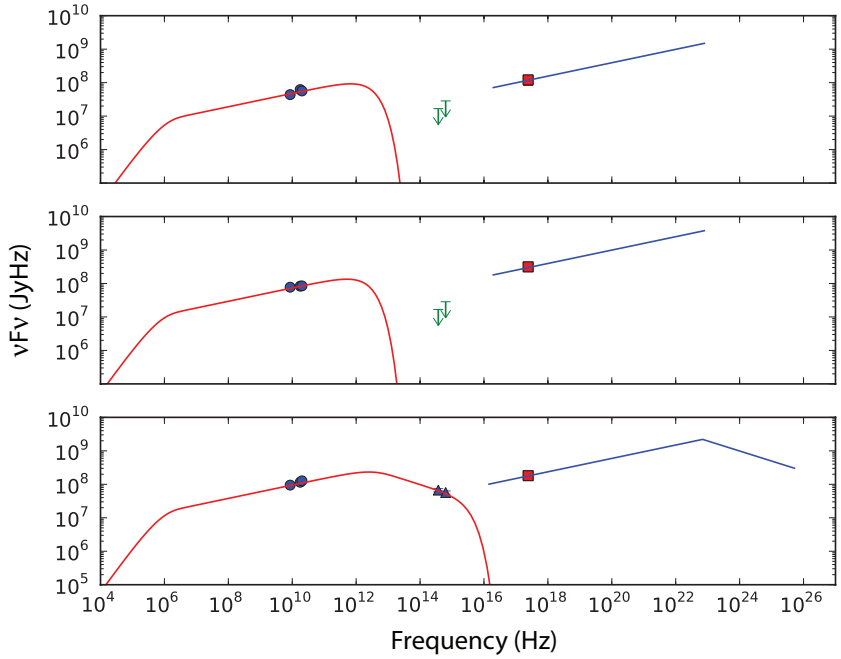

Figure 7. Spectral energy distributions for knots 3 (top), 4 (middle), and 6 (bottom). Also plotted are the synchrotron and analytic power-law model for the IC/CMB interpretation, with $\alpha = 0.8$, $\gamma_{\rm min} = 50$, and $\gamma_{\rm max} = 10^5$, and in the case of knot 6, a broken power-law model is used (see Section 5 for details). The parameters for the fits are given in Table 4. Note that while the x-ray spectral index of individual knots could not be measured, the x-ray spectral index of the entire jet is $\alpha^{7\,\rm keV}_{0.5\,\rm keV} = 0.85 \pm 0.2$, consistent with the slope of the model in the x-ray band.
(A color version of this figure is available in the online journal.)

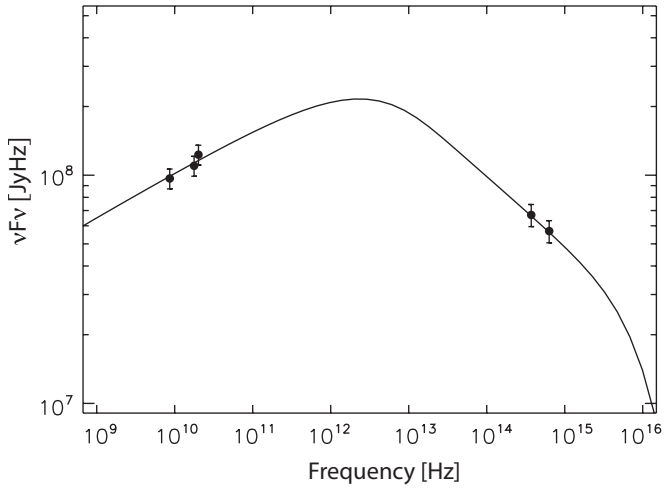

Figure 8. Broken power-law synchrotron spectrum fit to the radio to optical spectral energy distribution of knot 6. The relevant parameters of the fit are $\alpha = 0.8$, $\nu_b = 7 \times 10^{12}$ Hz, and $\nu_{\rm max} = 10^{16}$ Hz.

density per unit Lorentz factor, $N(\gamma) = K_e \gamma^{-a}$). The electrons cool as a result of synchrotron and IC emission downstream of the shock over a length D, which defines the extent of the emitting region. In this model, we assume that the post-shock magnetic field and velocity are uniform; this is a reasonable assumption for an oblique shock. An electron with Lorentz factor γ cools as a result of synchrotron and IC emission according to

$$\frac{d\gamma}{dt'} = -\xi\, \gamma^2 \tag{10}$$

where t' is time in the plasma co-moving frame,

$$\xi = \frac{4}{3}\frac{\sigma_T}{m_e c}\left(\frac{B^2}{8\pi} + U_{\rm CMB}\right), \tag{11}$$

in c.g.s. units, and the energy density of the CMB in the plasma co-moving frame is given by

$$U_{\rm CMB} = U_{\rm CMB,0}\,(1+z)^4\,\Gamma^2, \tag{12}$$

where the current epoch CMB energy density is $U_{\rm CMB,0} \approx 4.2 \times 10^{-13}$ erg cm^{-3} and Γ is the jet Lorentz factor.

The integrated emission from the post-shock region is the superposition of the emission from a number of progressively cooled slices. The volume-averaged number density per unit Lorentz factor is described by

$$\bar{N}(\gamma) = \begin{cases} 0 & \gamma < \gamma_{\rm min}, \quad \gamma > \gamma_{\rm max} \\ \frac{K_e \gamma_b}{(a-1)} \gamma^{-(a+1)} g\left(\frac{\gamma}{\gamma_b}\right) & \gamma_{\rm min} < \gamma < \gamma_{\rm max} \end{cases} \tag{13}$$

where

$$g\left(\frac{\gamma}{\gamma_b}\right) = \begin{cases} 1 - \left(1 - \frac{\gamma}{\gamma_b}\right)^{a-1} & \gamma < \gamma_b \\ 1 & \gamma > \gamma_b. \end{cases} \tag{14}$$

The break Lorentz factor γ_b is given by

$$\gamma_b = \frac{c}{\xi D}\Gamma_{\rm sh}\beta_{\rm sh}, \tag{15}$$

where $\beta_{\rm sh}$ is the velocity of plasma relative to the shock and $\Gamma_{\rm sh}$ is the corresponding Lorentz factor. The electron Lorentz factor γ_b is the Lorentz factor to which an electron of initially infinite energy cools following the shock. If the jet shock is stationary, then $\Gamma_{\rm sh} = \Gamma$.

The electron distribution (13) describes a broken power-law spectrum with the electron spectral index smoothly changing from a to $(a + 1)$ at $\gamma \approx \gamma_b$. The corresponding synchrotron spectrum is a broken power law with spectral index smoothly changing from α to $\alpha + 0.5$ at a frequency in the observer's frame,

$$\nu_b = \frac{\delta}{(1+z)} \frac{3}{4\pi} \Omega_0 \gamma_b^2, \quad (16)$$

where $\Omega_0 (= \frac{q_e B}{m_e c}$ in c.g.s. units) is the non-relativistic gyro-frequency. This equation relates the break frequency to the break Lorentz factor, and it is the break frequency, ν_b, that is actually used in the fit; the other parameter is the injected spectral index, $\alpha = (a-1)/2$. The values for the magnetic field $B \approx 30\,\mu$G and Doppler factor $\delta \approx 6$ have previously been determined from the relationship between x-ray and radio emission in Section 3.2.2. In order to minimize the number of parameters, we assume that $\Gamma = \delta$ in the following analysis.

We can compare the fitted break frequency with the value theoretically implied by Equation (15) for γ_b and (16) for ν_b. The theoretical break frequency is

$$\nu_b = \frac{27}{64\pi} \frac{\delta}{1+z} \frac{\Omega_0 m_e^2 c^4}{D^2 \sigma_T^2} \frac{\Gamma_{\rm sh}^2 \beta_{\rm sh}^2}{U^2}, \quad (17)$$

where $U = U_{\rm B} + U_{\rm CMB}$ is the total magnetic plus radiation energy density. The jet parameters derived from the IC/CMB model for this knot imply that IC losses dominate over synchrotron losses, since the CMB energy density in the jet rest frame is greater than the magnetic energy density. In order to compare the predicted break frequency with that determined by the synchrotron model, we need to estimate the length, D, of the emitting region. The radio image of knot 6 is found to be elongated in the jet direction with de-convolved (intrinsic) length $D \approx 0\farcs6$. The upper limit to the size of the x-ray knot is $0\farcs6$. The maximum allowed viewing angle for $\delta = 6$ is $\theta_{\rm max} \approx 9^\circ$, therefore, we take the de-projected knot length to be of order $D \approx 0\farcs6/\sin\theta_{\rm max} \approx 4'' \approx 30$ kpc $\approx 9 \times 10^{22}$ cm. If we adopt $D \approx 10^{23}$ cm and insert in Equation (17) the appropriate parameter values from the IC/CMB fit we obtain a predicted break frequency of 1.2×10^{13} Hz. This is less than a factor of two above the modeled value of 7×10^{12} Hz. Hence, the jet parameters derived from IC/CMB modeling of knot 6 are broadly consistent with the break frequency estimated by fitting a broken power law to the radio and optical data points.

We note that the *F814W HST* image of knot 6 (Figure 3) contains a double-peaked appearance, suggesting that a one-zone model of the emission region, which spans $\gtrsim$30 kpc in the radio band, may not be applicable.

6. X-RAY SPECTRAL ANALYSIS OF THE QUASAR CORE

X-ray events were extracted using a circular aperture of radius $2''$ centered on the core peak position. A total of 3687 events were extracted with energies in the range 0.5–7 keV. The pile-up fraction is estimated using the PIMMS Proposal Planning Toolkit to be 2% and is therefore neglected in the following analysis. The pulse-height amplitude spectrum was re-binned to have a minimum of 20 counts bin^{-1}, so that the χ^2 statistic could be applied.

The spectrum was fitted using an absorbed power-law model, with H I column density fixed at the Galactic value $N_{\rm H\,I} = 3.41 \times 10^{20}$ cm^{-2} as determined from the COLDEN column density calculator provided by the *Chandra* X-ray Center. The data, along with the best-fit curve, are shown in Figure 9. The parameters of the best fit are $\alpha_{\rm X-ray} = 0.84 \pm 0.05$, $S = 87 \pm 3$ nJy at 1 keV, and chi-squared per degree of freedom χ^2/d.o.f. $= 146.4/147 \approx 1.00$.

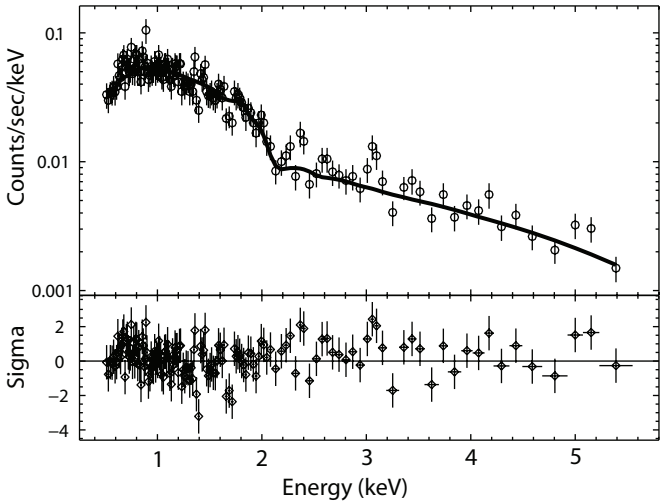

Figure 9. Observed ACIS-S spectrum of the core of PKS 2101−490 with model spectrum (absorbed power-law) overlaid. Also shown are the residuals of the fit, expressed as [(data − model)/error] in each bin. The positive residuals at approximately 3.1 keV may be associated with a 6.4 keV Fe Kα line redshifted by $z = 1.04$, consistent with the spectroscopic redshift (Marshall et al. 2005; J. Gelbord & H. L. Marshall, in preparation).

Marshall et al. (2005) reported a redshift of $z = 1.04$ for this source, based on an unpublished Magellan spectrum (see Section 1). We note positive residuals consistent with a 6.4 keV Fe Kα line redshifted by $z \approx 1.04$. If we include a line in the chi-squared fit, then the model parameters become $\alpha_{\rm X-ray} = 0.85 \pm 0.05$, $S = 87 \pm 3$ nJy at 1 keV, and the chi-squared per degree of freedom becomes χ^2/d.o.f. $= 134.7/145 \approx 0.93$. Although an F test would indicate that the line is significant, Protassov et al. (2002) show that such a test is not applicable to adding a spectral line to our basic model, and we have not carried out the extensive Monte Carlo testing they recommend since the jet physics is the primary result of this paper.

7. LOBES

Within the lobes, the radiation energy density of the CMB ($U_{\rm CMB} = 7 \times 10^{-12}$ erg cm^{-3}) is greater than the energy density of the locally generated synchrotron radiation. We therefore model the x-ray emission from the radio lobes in terms of IC scattering of the CMB, in this case assuming $\delta = 1$. In modeling the radio lobe emission, we assume a broken power-law electron energy distribution of the form given by Equation (13). The value for the break Lorentz factor γ_b is constrained by the x-ray spectrum. We argue as follows. The radio spectral index of the lobe is $\alpha_{\rm r} = 1.05 \pm 0.1$. We therefore assume that the radio emission corresponds to the post-break region of the electron spectrum. We assume a low-energy electron index, $a = 2.1$, so that the slope of the model synchrotron spectrum above the break matches the observed radio spectral index. The x-ray spectral index in the lobe is $\alpha_{\rm X-ray} = 1.3 \pm 0.3$. The IC x-ray emission in the *Chandra* x-ray band (0.5–7 keV) is produced by $\gamma \approx$ 600–2000 electrons, given that the scattered photons are CMB photons with an average energy $\approx 3.6\,\gamma^2\,kT_{\rm CMB}\,(1+z)$, where $T_{\rm CMB} \approx 2.7$ K is the current epoch temperature of the

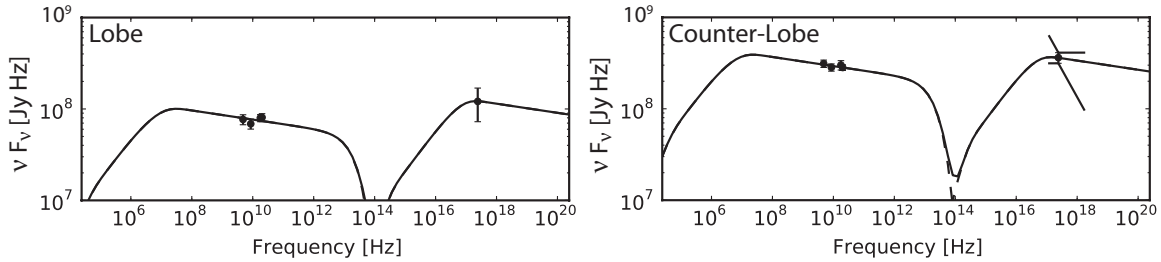

Figure 10. Lobe and counter-lobe spectral energy distributions. The solid lines are the best-fit synchrotron plus IC/CMB model. The parameters of the best-fit models are given in Table 6. The "bow-tie" around the counter-lobe x-ray data point illustrates the constraint on the x-ray spectral index of $\alpha_x = 1.3 \pm 0.3$. There are not enough x-ray counts in the lobe to provide meaningful constraints on the spectral index. However, in modeling the lobe SED, we have assumed the same x-ray spectral index as the counter lobe.

Table 6
Parameters of Model Fits to the Lobe Spectra

	Volume (cm^3)	α	γ_{min}	γ_b	γ_{max}	K_e (cm^{-3})	B (μG)	B_{min} (μG)
Counter lobe	9×10^{69}	0.55	10	500	6×10^5	1×10^{-5}	14	29
Lobe	4×10^{69}	0.55	10	500	6×10^5	0.8×10^{-5}	13	25

CMB. The steep x-ray spectrum therefore indicates that the Lorentz factor corresponding to the cooling break must be $\gamma_b \lesssim 600$. Hence, we adopt $\gamma_b = 500$. Given the unknown jet viewing angle, we assume projected volumes in the analysis. If the jet is angled close to the line of sight, as required by the IC/CMB model for jet x-ray emission, the volumes may be underestimated by a factor of 5–10. Larger volumes would imply closer agreement with the equipartition model.

Figure 10 shows the model fit to the radio and x-ray data for the lobe and counter lobe. The best-fit parameter values are given in Table 6, along with the minimum energy magnetic field strength calculated using standard expressions (e.g., Worrall & Birkinshaw 2006). The magnitude of the average magnetic field strength, as well as the ratio of B to B_{min}, is typical of powerful radio galaxies (Croston et al. 2005).

The presence of a low value for the break Lorentz factor ($\gamma_b \lesssim 500$) indicates an old source. However, enhanced IC cooling leads to a shorter cooling time than for radio galaxies at the current epoch. The cooling time for electrons of Lorentz factor γ in a magnetic field B (and hence magnetic energy density U_B) and immersed in the microwave background radiation with energy density U_{CMB} is

$$t_{cool} = \frac{m_e c}{\sigma_T} U_{CMB}^{-1} \left(1 + \frac{U_B}{U_{CMB}}\right)^{-1} \gamma^{-1}$$
$$\approx 3.6 \times 10^8 \left(1 + \frac{U_B}{U_{CMB}}\right)^{-1} \left(\frac{\gamma}{500}\right)^{-1} \text{yr} \quad (18)$$

for a microwave background temperature $(1+z) \times 2.725$ K. For the estimated lobe magnetic field strength, $U_B \approx U_{CMB}$, and $\gamma_b \sim 500$, implying a source age $t_{age} \lesssim 2 \times 10^8$ yr. Adiabatic losses would increase the cooling rate, meaning the above prediction may be an overestimate of the source age, hence the inequality in the estimate of t_{age} given above. For a deprojected jet length $\gtrsim$500 kpc (viewing angle $\lesssim 9^\circ$ as required by the beamed, equipartition IC/CMB model for jet x-ray emission), this implies a source expansion speed $\gtrsim 0.01\,c$. This estimate does not differ greatly from the estimate of the typical expansion speeds of lobes of a few percent of the speed of light (Scheuer 1995).

8. CONCLUSIONS

We have presented an analysis of new *Chandra*, *HST*, and ATCA images for the quasar jet source PKS 2101−490. We extracted the radio to x-ray spectral energy distributions from seven regions of the 13″ jet, and modeled the jet x-ray emission in terms of Doppler beamed IC scattering of the CMB (IC/CMB) for a jet in a state of equipartition between magnetic and particle energy densities (Section 3). Using this model, we derived a bulk Lorentz factor $\Gamma \sim 6$ and magnetic field strength of the order of 30 μG.

A major goal of this work has been to assess the validity of the beamed, equipartition IC/CMB model for jet x-ray emission through the use of additional constraints: namely, independent estimates of jet power, and the location of an apparent cooling break in the synchrotron spectrum of one of the jet knots. Below, we discuss the results of our analysis for each of these additional constraints.

The jet power predicted by the Doppler beamed, equipartition IC/CMB model was found to be in good agreement with independent order-of-magnitude estimates of jet power for this object, provided that $\gamma_{min} \sim 50$ in the jet, and the knots are significantly longer than the jet width, as implied by deprojection of the observed knot lengths (Section 4).

The brightest x-ray knot was detected in two *HST* filters, and the radio to optical data points were modeled as a broken power law with a standard cooling break $\Delta\alpha = 0.5$. The inferred break frequency was found to be consistent with the break frequency predicted using the IC/CMB model parameters along with the de-projected knot length that is implied by the small jet viewing angle required by the IC/CMB model (Section 5). However, we noted sub-structure in the *F814W HST* image of the bright optical knot, which is incompatible with a simple one-zone continuous injection model.

Finally, we note positive residuals consistent with a 6.4 keV Fe Kα line redshifted by the estimated $z = 1.04$ reported by Marshall et al. (2005).

L.E.H.G thanks the Grote Reber Foundation for financial support during part of this work. H.L.M., E.S.P., and J.G. acknowledge the support of HST grant GO-10352. D.A.S. is supported by NASA contract NAS8-03060 and CXC grant GO9-0121B. The Australia Telescope Compact Array is part of the Australia Telescope which is funded by the Commonwealth of Australia for operation as a National Facility managed by CSIRO. We gratefully acknowledge the anonymous referee for their comments which helped to improve and clarify the manuscript.

Facilities: ATCA, *CXO*, *HST*

REFERENCES

Atoyan, A., & Dermer, C. D. 2004, ApJ, 613, 151
Bicknell, G. V., Dopita, M. A., & O'Dea, C. P. O. 1997, ApJ, 485, 112
Celotti, A., Ghisellini, G., & Chiaberge, M. 2001, MNRAS, 321, L1
Chartas, G., Worrall, D. M., Birkinshaw, M., et al. 2000, ApJ, 542, 655
Croston, J. H., Hardcastle, M. J., Harris, D. E., et al. 2005, ApJ, 626, 733
Dermer, C. D. 1995, ApJ, 446, L63
Dickey, J. M., & Lockman, F. J. 1990, ARA&A, 28, 215
Double, G. P., Baring, M. G., Jones, F. C., & Ellison, D. C. 2004, ApJ, 600, 485
Ekers, J. A. 1969, Aust. J. Phys. Astrophys. Suppl., 7, 3
Fernandes, C. A. C., Jarvis, M. J., Rawlings, S., et al. 2011, MNRAS, 411, 1909
Gelbord, J. M., Marshall, H. L., Worrall, D. M., et al. 2005, ApJ, 632, L75
Georganopoulos, M., & Kazanas, D. 2004, ApJ, 604, L81
Gilliland, R. L. 2004, Instrument Science Report ACS 2004-01, 17, 18 pp
Godfrey, L. E. H. 2009, PhD thesis, Australian National Univ.
Godfrey, L. E. H., Bicknell, G. V., Lovell, J. E. J., et al. 2009, ApJ, 695, 707
Hardcastle, M. J. 2006, MNRAS, 366, 1465
Hardcastle, M. J., Evans, D. A., & Croston, J. H. 2007, MNRAS, 376, 1849
Hardcastle, M. J., Harris, D. E., Worrall, D. M., & Birkinshaw, M. 2004, ApJ, 612, 729
Harris, D. E., & Krawczynski, H. 2002, ApJ, 565, 244
Jorstad, S. G., & Marscher, A. P. 2004, ApJ, 614, 615
Kataoka, J., & Stawarz, Ł. 2005, ApJ, 622, 797
Kenney, J. F., & Keeping, E. S. 1951, in The Mathematics of Statistics, Part 2, The Distribution of the Standard Deviation (2nd ed.; Princeton, NJ: Van Nostrand), 170
Krist, J. E., & Burrows, C. J. 1994, WFPC2 ISR 94-01
Krist, J. E., & Hook, R. 2004, The TinyTim Users Guide, Version 6.3, http://www.stsci.edu/software/tinytim/tinytim.pdf
Large, M. I., Mills, B. Y., Little, A. G., Crawford, D. F., & Sutton, J. M. 1981, MNRAS, 194, 693
Lobanov, A. P. 1998, A&A, 330, 79
Lovell, J. E. J. 1997, PhD thesis, Univ. Tasmania
Lovell, J. E. J., Tingay, S. J., Piner, B. G., et al. 2000, in Astrophysical Phenomena Revealed by Space VLBI, ed. H. Hirabayashi, P. G. Edwards, & D. W. Murphy (Sagamihara: ISAS), 215
Marshall, H. L., Gelbord, J. M., Schwartz, D. A., et al. 2011, ApJS, 193, 15
Marshall, H. L., Harris, D. E., Grimes, J. P., et al. 2001, ApJ, 549, L167
Marshall, H. L., Schwartz, D. A., Lovell, J. E. J., et al. 2005, ApJS, 156, 13
Massaro, F., Harris, D. E., & Cheung, C. C. 2011, ApJS, 197, 24
Mauch, T., Murphy, T., Buttery, H. J., et al. 2003, MNRAS, 342, 1117
Mehta, K. T., Georganopoulos, M., Perlman, E. S., Padgett, C. A., & Chartas, G. 2009, ApJ, 690, 1706
Meisenheimer, K., Roser, H.-J., Hiltner, P. R., et al. 1989, A&A, 219, 63
Mueller, M., & Schwartz, D. A. 2009, ApJ, 693, 648
Mullin, L. M., & Hardcastle, M. J. 2009, MNRAS, 398, 1989
Norman, M. L. 1996, in ASP Conf. Ser. 100, Energy Transport in Radio Galaxies and Quasars, ed. P. E. Hardee, A. H. Bridle, & J. A. Zensus (San Francisco, CA: ASP), 319
Perlman, E. S., Georganopoulos, M., Marshall, H. L., et al. 2011, ApJ, 739, 65
Protassov, R., van Dyk, D. A., Connors, A., Kashyap, V. L., & Siemiginowska, A. 2002, ApJ, 571, 545
Rawlings, S., & Saunders, R. 1991, Nature, 349, 138
Sambruna, R. M., Gambill, J. K., Maraschi, L., et al. 2004, ApJ, 608, 698
Sambruna, R. M., Maraschi, L., Tavecchio, F., et al. 2002, ApJ, 571, 206
Sambruna, R. M., Urry, C. M., Tavecchio, F., et al. 2001, ApJ, 549, L161
Scheuer, P. A. G. 1995, MNRAS, 277, 331
Schlegel, D. J., Finkbeiner, D. P., & Davis, M. 1998, ApJ, 500, 525
Schwartz, D. A. 2002, ApJ, 569, L23
Schwartz, D. A., Marshall, H. L., Lovell, J. E. J., et al. 2000, ApJ, 540, L69
Schwartz, D. A., Marshall, H. L., Lovell, J. E. J., et al. 2006a, ApJ, 640, 592
Schwartz, D. A., Marshall, H. L., Lovell, J. E. J., et al. 2006b, ApJ, 647, L107
Schwartz, D. A., Massaro, F., Siemiginowska, A., et al. 2010, Int. J. Mod. Phys. D, 19, 879
Siemiginowska, A., Bechtold, J., Aldcroft, T. L., et al. 2002, ApJ, 570, 543
Siemiginowska, A., Stawarz, Ł., Cheung, C. C., et al. 2007, ApJ, 657, 145
Sirianni, M., Jee, M. J., Benítez, N., et al. 2005, PASP, 117, 1049
Stawarz, Ł., Sikora, M., Ostrowski, M., & Begelman, M. C. 2004, ApJ, 608, 95
Suchkov, A., & Krist, J. 1998, Instrument Science Report NICMOS 98-018, 18, 11 pp
Tavecchio, F., Ghisellini, G., & Celotti, A. 2003, A&A, 403, 83
Tavecchio, F., Maraschi, L., Sambruna, R. M., & Urry, C. M. 2000, ApJ, 544, L23
Walker, R. C. 1995, in ASP Conf. Ser. 82, Very Long Baseline Interferometry and the VLBA, ed. J. A. Zensus, P. J. Diamond, & P. J. Napier (San Francisco, CA: ASP), 133
Wardle, J. F. C., & Aaron, S. E. 1997, MNRAS, 286, 425
Willott, C. J., Rawlings, S., Blundell, K. M., & Lacy, M. 1999, MNRAS, 309, 1017
Wilson, A. S., Smith, D. A., & Young, A. J. 2006, ApJ, 644, L9
Wilson, A. S., Young, A. J., & Shopbell, P. L. 2000, ApJ, 544, L27
Worrall, D. M., & Birkinshaw, M. 2006, in Lecture Notes in Physics, Vol. 693, Physics of Active Galactic Nuclei at all Scales, ed. D. Alloin, R. Johnson, & P. Lira (Berlin: Springer), 39
Worrall, D. M. 2009, A&AR, 17, 1
Wright, A., & Otrupcek, R. 1990, PKS Catalog (1990), 0